Tomographic diffractive microscopy with isotropic resolution

BERTRAND SIMON[1], MATTHIEU DEBAILLEUL[1], MOUNIR HOUKAL[2], CAROLE ECOFFET[2], JONATHAN BAILLEUL[1], JOËL LAMBERT[1], ARNAUD SPANGENBERG[2], HUI LIU[3], OLIVIER SOPPERA[2] AND OLIVIER HAEBERLÉ[1,*]

[1]*Laboratoire Modélisation Intelligence Processus et Systèmes MIPS – EA2332, Université de Haute-Alsace (UHA), 61 rue Albert Camus F-68093 Mulhouse Cedex, France*
[2]*Institut de Science des Matériaux de Mulhouse IS2M, Université de Haute-Alsace (UHA), CNRS UMR 7361,15 rue Jean Starcky, BP 2488, F-68057 Mulhouse Cedex, France*
[3]*Institut de Génétique et de Biologie Moléculaire et Cellulaire IGBMC, Université de Strasbourg (UniStra), CNRS UMR 7104, INSERM U964, 1 rue Laurent Fries, F-67404 Illkirch Cedex, France*
**Corresponding author: olivier.haeberle@uha.fr*

Received XX Month XXXX; revised XX Month, XXXX; accepted XX Month XXXX; posted XX Month XXXX (Doc. ID XXXXX); published XX Month XXXX

Microscopy techniques allowing for observation of unlabeled samples have recently known a regain of interest. In particular, approaches based on recording of the optical field diffracted by the specimen, in amplitude and phase, have proven their capacities for biological investigations. When combined with variations of the specimen illumination, tomographic acquisitions are possible. One limitation of previously developed approaches is the anisotropic resolution, characteristic of all transmission microscopes. In this context, an instrument, characterized by isotropic high-resolution three-dimensional imaging capabilities, is still awaited. For the first time, we have developed tomographic diffractive microscopy combining specimen rotation and illumination rotation, which delivers images with (almost) isotropic resolution below 200 nm. The method is illustrated by observations of nanoscopic fiber tips, microcrystals and pollens, and should be helpful for characterizing freestanding natural (diatoms, spores, red- or white blood cells…) or artificial samples.

OCIS codes: *(180.0180) Microscopy; (180.6900) Three-dimensional microscopy; (180.3170) Interference microscopy; (090.0090) Holography; (090.1995) Digital holography; (090.2880) Holographic interferometry.*

http://dx.doi.org/10.1364/optica.99.099999

Fluorescence microscopy is the tool of choice for functional investigations, thanks to the immense variety of labels, and to the development of fluorescence nanoscopy, recognized by the attribution of the Nobel Prize in Chemistry 2014 for the development of super-resolved fluorescence microscopy. But for scientists who do not want to, or cannot use fluorescence or electron microscopy, imaging capabilities of conventional optical microscopes are still limited.

Among the various techniques developed to image non-fluorescent samples, phase microscopy has already found many applications, in biology as well as material science [1-5].

Tomographic diffractive microscopy [6-14] (TDM, also referred as synthetic aperture microscopy, tomographic phase microscopy, phase nanoscopy, optical diffraction tomography…, see Ref. [14] for a general introduction to these techniques) is an extension of phase microscopy, combining amplitude and phase imaging with a variation of the conditions of illumination and/or the conditions of observation. It relies on computer-assisted image reconstruction of the sample, from the electromagnetic field it diffracts. The simplest approach considers that first Born approximation is valid, so that the diffracted field is linked to the 3-D Fourier transform of the specimen index of refraction distribution [15].

Figure 1 describes the acquisition process for common holographic and tomographic configurations, highlighting the interest of this technique, in terms of sample frequencies acquisition. In Fourier domain of spatial frequencies, the diffracted field is represented by the k_{diff} wavevectors depicting the Ewald sphere. In holographic microscopy, one direction of illumination, usually parallel to the optical axis (depicted by k_{ill} vector), is used, and because of the limited numerical aperture (NA) of the microscope objective, only a cap of sphere of k_{diff} vectors is detected (Fig. 1(a)). The elastic scattering condition links the registered field to specimen frequencies by momentum conservation $k_{obj} = k_{diff} - k_{ill}$. While the lateral extension of the k_{obj} cap of sphere provides a good lateral resolution, its axial extension being very restricted, the imaging capabilities along the optical axis are strongly affected [8-12].

To improve the resolution, one can use inclined illumination [6-12], shifting detected k_{diff} vectors towards higher k_{obj} vectors (Fig. 1(b)). When many illuminations are sequentially used, a virtual condenser is synthetized, and the Optical Transfer Function (OTF) support is extended, and filled [6] (Fig. 1(c)). The lateral and axial resolutions are improved, and true 3-D imaging becomes possible [8-12]. However, the smaller extension of the OTF along k_z-direction (optical axis) and the so-called "missing cone" translates into lower axial resolution, and limit sectioning capabilities [12], as for any transmission microscope.

Another approach consists in rotating the sample (Fig. 1(d)): an almost complete spherical OTF is obtained, albeit with smaller extension, and a small set of missing frequencies does exist along the rotation axis [16] (here y-axis), slightly degrading the resolution in this direction [17]. This configuration also requires a large number of sample rotations to properly fill the OTF [17-19].

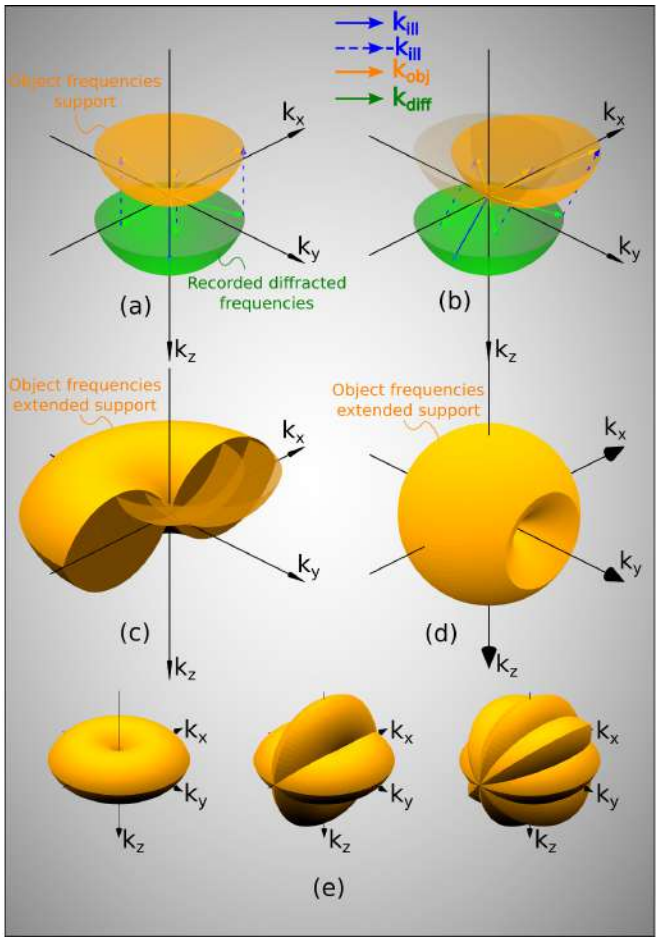

Fig. 1: Construction of the Optical Transfer Function (OTF) for various configurations of tomographic diffractive microscopy. (a): digital holographic microscopy. The recorded k-vectors k_{diff} are shifted back according to the momentum conservation to provide object vectors k_{obj}: the OTF depicts a cap of sphere of large lateral, but limited longitudinal extension. (b): when using inclined illumination in TDM with illumination rotation (TDM-IR), same positions of k_{diff} vectors provide new k_{obj} vectors. (c) a large set of illuminations results in a filled and extended OTF: TDM-IR provides improved-resolution, higher-quality 3-D images. Note however the presence of a so-called "missing cone" along the optical axis z, limiting longitudinal resolution and sectional capabilities. (d): OTF for TDM with specimen-rotation (TDM-SR). An almost completely filled sphere is obtained, but of lesser extension than in the previous case. (e): OTFs for TDM-IR-SR obtained when combining TDM-IR with 0°, (0°;90°), and (0°;45°;90°;135°) specimen rotations, respectively (displayed at half scale compared to Fig. 1(a-d)). A missing-cone free and extended support is obtained, showing that TDM-IR-SR can deliver 3-D, isotropic- and improved resolution images. See also Visualization 1.

In order to simultaneously obtain improved- and isotropic-resolution images, one can combine [13] illumination and specimen rotations. Figure 1(e) shows the OTF support for 1, 2 and 4 views: few rotations permit to obtain a quasi-spherical, extended OTF (see also Visualization 1 for an animated construction of the frequency supports). Theoretically proposed in Ref. [13] and studied by simulations, such a configuration had however not been experimentally tested up to now. The lateral and axial extensions of the frequency support for holographic microscopy are given by [6]:

$$\Delta\nu_{x,y}^{Holo} = \frac{2n\sin\theta}{\lambda} \quad \Delta\nu_{z}^{Holo} = \frac{n(1-\cos\theta)}{\lambda}$$

For TDM with illumination rotation (TDM-IR), one doubles the lateral frequency support [6] and

$$\Delta\nu_{x,y}^{TDM-IR} = \frac{4n\sin\theta}{\lambda} \quad \Delta\nu_{z}^{TDM-IR} = \frac{2n(1-\cos\theta)}{\lambda}$$

For TDM with sample rotation (TDM-SR), one gets [13]:

$$\Delta\nu_{x,z}^{TDM-SR} = \frac{4n\sin(\theta/2)}{\lambda} \quad \Delta\nu_{y}^{TDM-SR} = \frac{2n\sin\theta}{\lambda}$$

When combining both approaches (TDM-IRSR), one obtains:

$$\Delta\nu_{x,y,z}^{TDM-IRSR} = \frac{4n\sin\theta}{\lambda}$$

To overcome the resolution limitations of previously developed TDM systems [6-12, 17-19], we have developed TDM-IRSR by adapting a special sample rotation system, compatible with high numerical aperture objective and condenser (NA_{obj} = NA_{con} = 1.4), onto our previously built TDM-IR system. The system is based on a modified Mach-Zehnder interferometer, the angle of incidence of the illumination beam (633 nm or 475 nm) being controlled using a fast tip-tilt mirror. The diffracted- and reference beams are recombined prior detection, in off-axis configuration. Interferograms are corrected for residual aberrations [20], and merged in Fourier space. Image reconstruction can be performed under Born or Rytov approximation (see also Supplement 1 for more details about experimental setup).

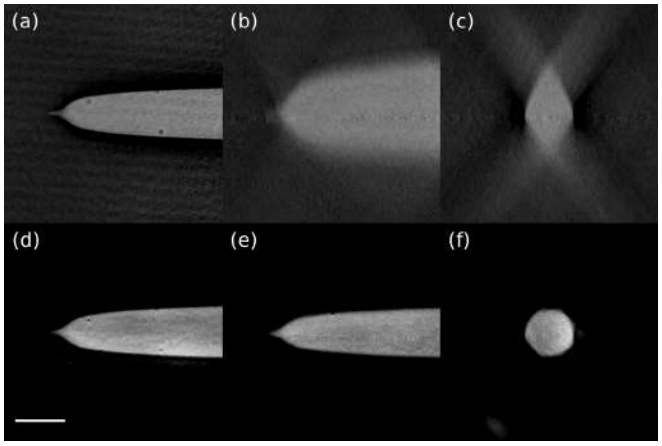

Fig. 2: Lateral, axial and sagittal views of a tapered fiber tip, obtained by heat-and-pull technique, and observed with tomographic diffractive microscopy. (a): with TDM-IR. (x-y) lateral plane view: note the excellent lateral resolution. (b): (x-z) axial plane view: the missing-cone in this configuration induces low resolution along the optical axis, and the fiber tip is not visible. (c): (y-z) sagittal view: the low sectional capabilities of TDM-IR translate into a deformed image of the specimen: the fiber section is not circular. (d-f) same fiber observed with TDM-IR-SR. The fiber tip is now clearly visible on both (x-y) and (x-z) views, and the fiber section is almost circular, as expected. Combination of four acquisitions after specimen rotation of 0°, 54°, 90°, and 126° steps, respectively. Scale bar: 3 µm.

To illustrate the superior imaging capabilities of this new instrument, a tapered optical fiber is first imaged with 475 nm illumination. The heat-and-pull technique [21] produces very sharp tips, a few micrometers long, and with a tip end diameter below 100 nm. These characteristics make of such an object a good test pattern to compare the quality of the images obtained from different configurations.

Figures 2(a,b,c) show (x-y), (x-z), and (y-z) views, respectively, of the 3-D image of the fiber tip, obtained in TDM-IR. The high lateral resolution permits to observe the 1 µm long fiber tip on the (x-y) view. On Fig. 2(a), a 95 nm resolution (or $\lambda/3.5NA$, as in Ref. [8]) is estimated (with classical lateral resolution in incoherent imaging: $R_{lat} = \lambda/2NA$ = 170 nm). Note that measuring resolution in coherent imaging may be challenging [22] and see Supplement 1 for details about resolution estimation. The system suffering from the previously mentioned z-axis elongation, the sharp tip is however not visible in the (x-z) view (Fig. 2(b). Furthermore, the fiber itself is not observed as a cylindrical object (Fig. 2(c)).

In order to perform TDM-IRSR, the fiber is connected to a stepper motor, to ensure rotation [23]. Figures 2(d-f) show the fiber, after combining 4 views obtained at 0°, 54°, 90° and 126°. The section of the fiber now almost depicts a disc, and the sharp tip is visible on both (x-y) and (z-y) views (see Supplement 1 for details about the data fusion procedure). A lateral resolution of 150 nm, and a longitudinal resolution of 180 nm are obtained (with classical longitudinal resolution: $R_{long} = n\lambda/(NA)^2$ = 490 nm). These indicate that the fusion process is not perfect, the lateral resolution being slightly degraded, but a large gain in longitudinal resolution is indeed obtained. Higher lateral resolutions have been reported [10,12], but such a high and (almost) isotropic resolution in transmission microscopy is a novelty, which constitutes a breakthrough in the domain, and should permit more precise investigations, for example at cellular level in biology.

To observe specimens, like pollens, diatoms, or microcrystals, we attach them to an optical fiber by photopolymerisation (Supplement 1 describes in detail the sample attachment procedure), the fiber being used both as sample holder and rotator.

Figures 3(d-h) illustrate image quality gain for a zeolite crystal imaged with one view, Fig. 3(d), and after fusion of 8 views. Note the microbubbles attached to the crystal, which appear spherical on Figs. 3(e,f), but noticeably elongated on Fig. 3(d) (see also Visualization 2): when imaging cells, precise shape and volume determination of smaller organelles could be hampered by this anisotropy when observed with TDM-IR (TDM-SR delivering anyway lower-resolution images), while TDM-IRSR would allow for much more precise measurements.

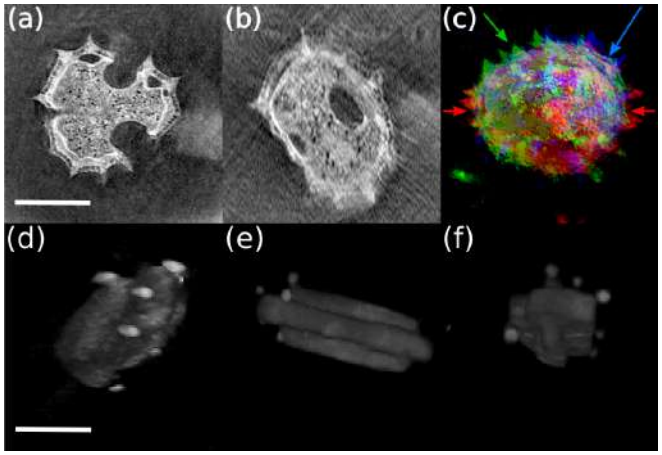

Fig. 3: Bellis perennis pollen grain and zeolite crystal observed with tomographic diffractive microscopy. (a) (x-y) view for one angle of acquisition (TDM-IR). The polymer fiber tip, used to rotate the sample is visible. Note the characteristic spikes of this type of pollen. (b) (x-z) view in TDM-IR. Note the elongation along the optical axis, and the vanishing aspect of the pollen surface, due to the missing cone. The spikes are hardly recognizable. (c) colored superimposition of three views of the same pollen grain for three angles of rotation of the sample (red: 0°, green: 54° and blue: 108°). Note the complementarity of the data (colored arrows): fusion should permit to deliver isotropic resolution images. Scale bar: 10 µm. (d-f): images of a zeolite crystal for (d): one angle of acquisition (TDM-IR) and (e,f) after 8 acquisitions and data fusion (TDM-IRSR). The crystal is better imaged, and the small surrounding bubbles attached to the crystal are spherical with TDM-IRSR, while they appear elongated with TDM-IR only. Scale bar: 10 µm. See also Visualization 2.

Figure 4 shows a Betula pendula triporate pollen grain. TDM delivers dual views of the sample, identifying refraction and absorption in two separate images [14]. The contact-sheet depicts volumetric cuts in the z direction (x-y views) through the index image, Fig. 4(a), and the absorption image, Fig. 4(b), highlighting the inner structures of the pollen grain, its double-layer outer structure (arrow) with chambers separating inner and outer walls (vestibulum), and protruding pores (double-headed arrow) (see also Visualization 3). The RI (Refraction Index) is calibrated from the known RIs of the immersion medium and of the photopolymer tip. The pollen walls are composed of highly refractive components like sporopollenins and cellulose [24], while the vestibulum is of lower RI. Some regions of the nucleus exhibit high RI [25], and the absorptive components seem confined to the interior of the pollen.

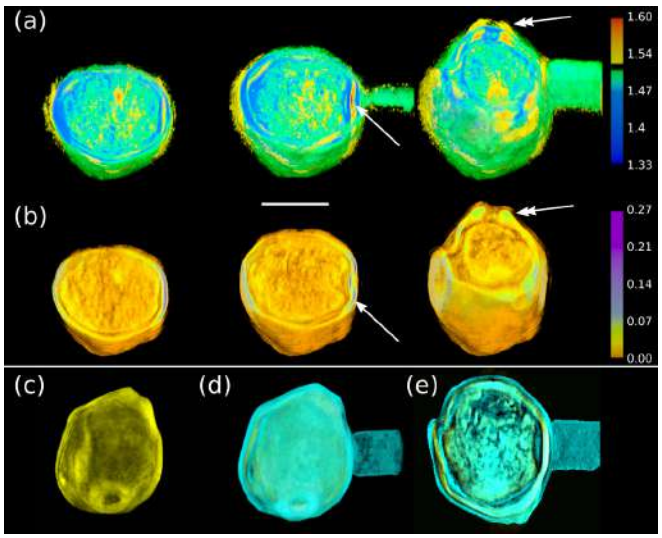

Fig. 4: Betula pollen grain observed with tomographic diffractive microscopy. (a), (b) volumetric cuts (x-y views) through the 3-D index of refraction image and the absorption image, respectively. Note the higher index of refraction of the pollen walls, especially near the pores (double-headed arrow), and the doubled outer wall (arrow). Scale bar: 10 µm. See also Visualization 3. (c): outer view of the pollen: image of the absorption component, displayed in yellow. (d): outer view of the pollen: image of the complex index of refraction, with refractive component displayed in cyan. The photopolymer tip used to handle the sample is purely refractive, hence visible on the index component, but not on the absorption image. (e): (x-y) cut through the pollen. Note that the absorptive components are confined to the interior of the pollen: nucleus and intine, and absent from the exine. See also Visualization 4.

Such clear discrimination between refractive and absorptive parts of a sample, in 3-D and at high resolution also constitute a novelty. While refraction images have proven to constitute a useful tool for biological investigations [7,9-11,26], absorption images have not been used up to now, but indeed give complementary information [8,12,27-29].

Figures 4(c,d) show 3D views of the absorption within the pollen, and of the complex index of refraction (refraction and absorption), respectively. Note the photopolymer tip, identifiable on Fig. 4(d), but not on Fig. 4(c). The absorption image (yellow) is indeed embedded within the refraction image (cyan), as shown on Fig. 4(e), which is a cut through the pollen: attenuation is confined to the inner wall or intine, while the outer wall, or exine,

is refractive only (see also Visualization 4). Finer characterization of pollen grain optical properties would for example be necessary in view of better understanding their contribution by direct absorption and scattering to local radiative forcing. Current models, even if geometrically very elaborate, usually neglect absorption [30]. The method we propose may contribute to address this limitation.

In conclusion, we have developed a tomographic diffractive microscope combining illumination and specimen rotations that circumvents an important limitation in transmission microscopy: it delivers images with an isotropic and improved resolution, and with also clear distinction of refraction and attenuation, two quantities, which are usually mixed in intensity-only microscopy [14]. Possible extensions of this technique include isotropic-resolution, combined TDM-fluorescence microscopy [12,28], and spectral TDM imaging [31], as attenuation is often strongly wavelength-dependent.

Biological research [1-5] on freestanding specimens (for example microplankton science, palynology, bacteriology, hematology, gamete and fertilization studies) as well as research on transparent materials [5] like photopolymers, structured optical fibers, textile fiber science, micro- and nanofabrication characterization, microcrystal could benefit from the superior imaging capabilities of such an instrument.

Using glass microcapillaries [17-19,25], or contact-free sample rotation systems, based on optical- [32,33] or dielectrophoretic forces [34,35] may also facilitate the use of this technique with living, freestanding samples, like red- or white blood cells, egg cells, pollens, or unicellular organisms (diatoms, radiolarians). For living specimens however, the oil immersion objectives used throughout this work should be replaced by water immersion objectives (with slightly lowered resolution).

Alternately, if observing larger inert samples, low numerical aperture, long working-distance air objectives could be used. For samples presenting high indices of refraction, the technique we have developed could also benefit from advanced numerical reconstruction methods, which allow for true superresolution in far-field microscopy [36].

Funding. French Agence Nationale de la Recherche: ANR-11-JS10-0003 OSIRIS: Optical-Scanning Isotropic-Resolution Imaging System and ANR-10-PDOC-0009 Nanoquenching.

See Supplement 1 for supporting content.

REFERENCES

1. K. Myung, *Digital Holographic Microscopy: Principles, Techniques, and Applications*, Springer Series in Optical Science Vol. 162, Springer, 2011
2. G. Popescu, *Quantitative Phase Imaging of Cells and Tissues*, McGraw Hill, 2011
3. K. Lee, K. Kim, J. Jung, J. Heo, S. Cho, S. Lee, G. Chang, Y. Jo, H. Park, and Y. Park, Sensors **13**, 4170 (2013)
4. B. Kemper, *Digital holographic microscopy: quantitative phase imaging and applications in live cell analysis*, in Handbook of Coherent-Domain Optical Methods, V. V. Tuchin, ed., Springer, 2013
5. B. Bhaduri, C. Edwards, H. Pham, R. Zhou, T. Nguyen, L. Goddard, and G. Popescu, Adv. Opt. and Phot. **6**, 57 (2014)
6. V. Lauer, J. Microscopy **205**, 165 (2002)
7. W. Choi, C. Fang-Yen, K. Badizadegan, S. Oh, N. Lue, R. R. Dasari, and M. S. Feld,, Nature Meth. **4**, 717 (2007)
8. M. Debailleul, B. Simon, V. Georges, O. Haeberlé, and V. Lauer, Meas. Sci. Technol. **19**, 074009 (2008)
9. Y. Park, M. Diez-Silva, G. Popescu, G. Lykotrafitis, W. Choi, M. S. Feld, and S. Suresh, Proc. Nat. Acad. Sci. USA **105**, 13730 (2008)
10. Y. Cotte, F. Toy, P. Jourdain, N. Pavillon, D. Boss, P. Magistretti, P. Marquet and C. Depeursinge, Nature Phot. **7**, 113 (2013)
11. T. Kim, R. Zhou, M. Mir, S. Derin Babacan, P. Scott Carney, L. L. Goddard, and G. Popescu, Nature Phot. **8**, 256 (2014)
12. M. Debailleul, V. Georges, B. Simon, R. Morin, and O. Haeberlé, Opt. Lett. **34**, 79 (2009)
13. S. Vertu, J. Flügge, J.-J. Delaunay, and O. Haeberlé, Centr. Eur. J. of Phys. **9**, 969 (2011)
14. O. Haeberlé, K. Belkebir, H. Giovannini and A. Sentenac, J. Mod. Opt. **57**, 686 (2010)
15. E. Wolf, Opt. Comm. **1**, 153 (1969)
16. S. Vertu, J.-J. Delaunay, I. Yamada, and O. Haeberlé, Centr. Eur. J. of Phys. **7**, 22 (2009)
17. Y.-C. Lin, and C.-J. Cheng, J. Opt. **16**, 065401 (2014)
18. M. Kujawińska, W. Krauze, A. Kus, J. Kostencka, T. Kozacki, B. Kemper, and M. Dudek, Int. J. of Optomechatronics **8**, 357 (2014)
19. A. Kus, M. Dudek, B. Kemper, M. Kujawińska, and A. Vollmer, J. Biom. Opt **19**, 46009 (2014).
20. H. Liu, J. Bailleul, B. Simon, M. Debailleul, B. Colicchio, and O. Haeberlé, Appl. Opt. **53**, 748 (2014)
21. M. Xiao, J. Nieto, J. Siqueiros, and R. Machorro, Rev. Sci. Instrum. **68**, 2787 (1997)
22. R. Horstmeyer, R. Heintzmann, G. Popescu, L. Waller, and C. Yang, Nature Phot. **10**, 68 (2016)
23. A. Barty, K. A. Nugent, A. Roberts, and D. Paganin, Opt. Comm. **175**, 329 (2000)
24. S. Barrier, *Physical and chemical properties of sporopollenin exine particles*, (Ph.D., University of Hull, 2008) https://hydra.hull.ac.uk/assets/hull:6412a/content
25. F. Charrière, A. Marian, F. Montfort, J. Kuehn, T. Colomb, E. Cuche, P. Marquet, and C. Depeursinge, Opt. Lett. **31**, 178 (2006)
26. K. Kim, S. Lee, J. Yoon, J. Heo, C. Choi, and Y. Park, Scientific Reports **6**, 36815 (2016)
27. T. C. Wedberg, and W. C. Wedberg, J. Microsc. **177**, 53 (1995)
28. B. Simon, M. Debailleul, A. Beghin, Y. Tourneur, and O. Haeberlé, J. Biophoton. **3**, 462 (2010)
29. K. Kim, H. Yoon, M. Diez-Silva, M. Dao, R. R. Dasari, and Y. Park, J. Biom. Opt. **19**, 011005 (2014)
30. C. Liu, and Y. Yin, Opt. Expr. **24**, A104 (2016)
31. J. Jung, K. Kim, J. Yoon, and Y. Park, Opt. Expr. **24**, 2006 (2016)
32. M. K. Kreysing, T. Kießling, A. Fritsch, C. Dietrich, Opt. Exp. **16**, 16984 (2008)
33. M. Habaza, B. Gilboa, Y. Roichman, and N. Shaked, Opt. Lett. **40**, 1881 (2015)
34. B. Le Saux, B. Ghalmond, Y. Yu, A. Trouvé, O. Renaud, and S. L. Shorte, J. Microsc. **233**, 404 (2009)
35. M. Habaza, M. Kirschbaum, C. Guernth-Marschner, G. Dardikman, I. Barnea, R. Korenstein, C. Duschl, and N. T. Shaked, Adv. Sci., 1600205 (2016)
36. T. Zhang, C. Godavarthi, P. Chaumet, G. Maire, H. Giovannini, A. Talneau, M. Allain, K. Belkebir, and A. Sentenac, Optica **3**, 609 (2016)

Tomographic diffractive microscopy with isotropic resolution: supplementary material

BERTRAND SIMON[1], MATTHIEU DEBAILLEUL[1], MOUNIR HOUKAL[2], CAROLE ECOFFET[2], JONATHAN BAILLEUL[1], JOËL LAMBERT[1], ARNAUD SPANGENBERG[2], HUI LIU[3], OLIVIER SOPPERA[2] AND OLIVIER HAEBERLÉ[1,*]

[1]*Laboratoire Modélisation Intelligence Processus et Systèmes MIPS – EA2332, Université de Haute-Alsace (UHA), 61 rue Albert Camus F-68093 Mulhouse Cedex, France*
[2]*Institut de Science des Matériaux de Mulhouse IS2M, Université de Haute-Alsace (UHA), CNRS UMR 7361,15 rue Jean Starcky, BP 2488, F-68057 Mulhouse Cedex, France*
[3]*Institut de Génétique et de Biologie Moléculaire et Cellulaire IGBMC, Université de Strasbourg (UniStra), CNRS UMR 7104, INSERM U964, 1 rue Laurent Fries, F-67404 Illkirch Cedex, France*
**Corresponding author: olivier.haeberle@uha.fr*

Published XX Month XXXX

This document provides supplementary information to "Full Ewald sphere tomographic diffractive microscopy with isotropic three-dimensional resolution", *Optica* volume, first page (year). It describes the experimental setup used to perform full Ewald sphere tomographic acquisitions, the method of resolution estimation, the fusion techniques to merge data, and the technique to attach samples, and perform specimens rotation.

http://dx.doi.org/10.1364/optica.99.099999.s1 [supplementary document doi]

1. Experimental setup

The principle of our tomographic diffractive microscopy with illumination rotation has been described in previous works [1-4]. For the present study, we have developed (see Fig. S1) a compact system, based on a Mach-Zehnder interferometer, from off-the-shelf opto-mechanical elements (Thorlabs).

A 10 mW, linear polarization, 633 nm HeNe laser (HNL100L-EC Thorlabs) is used as coherent source, for sample illumination and for reference beam generation via a beam splitter. Alternately, a 475 nm DPSS laser (B&W Tek BWB-475-10-OEM) can also be used.

A high numerical aperture objective (100x NA = 1.4 oil immersion Olympus) serves as a condenser, in conjunction with a fast steering mirror (FSM300 Newport) to perform angular scanning illumination. A second high numerical aperture objective (100x NA = 1.4 oil immersion Olympus) collects the diffracted field and forms the image.

The diffracted beam is recombined with the reference beam, and detected using a GigE interface, 1280x1024 pixels CMOS camera (PHF-MV1-D2048-96-G2 PhotonFocus).

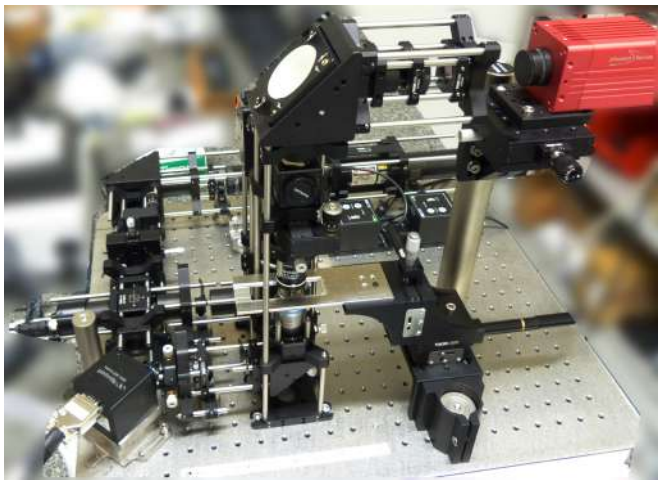

Figure S1: compact tomographic diffractive microscope with illumination rotation using high NA illumination and high NA detection, built from off-the-shelf elements.

The tip-tilt mirror, via a LabJack U12 module (LabJack), and the camera are triggered by the acquisition computer. Holograms are acquired at a rate of 96 frames/s, and typically 400 holograms are acquired for one 3-D tomographic reconstruction.
Reconstructions are performed at a rate of 3 s for one 3-D image using an Intel i7, 4 GHz Linux computer, equipped with 32Mb of memory. Image reconstructions are performed on-line, which permits to immediately visualize the observed sample.
The sample is translated via an x-y motorized scanning stage. Focus can be performed optically, via a manual z-stage, and numerically, by computing hologram propagation.

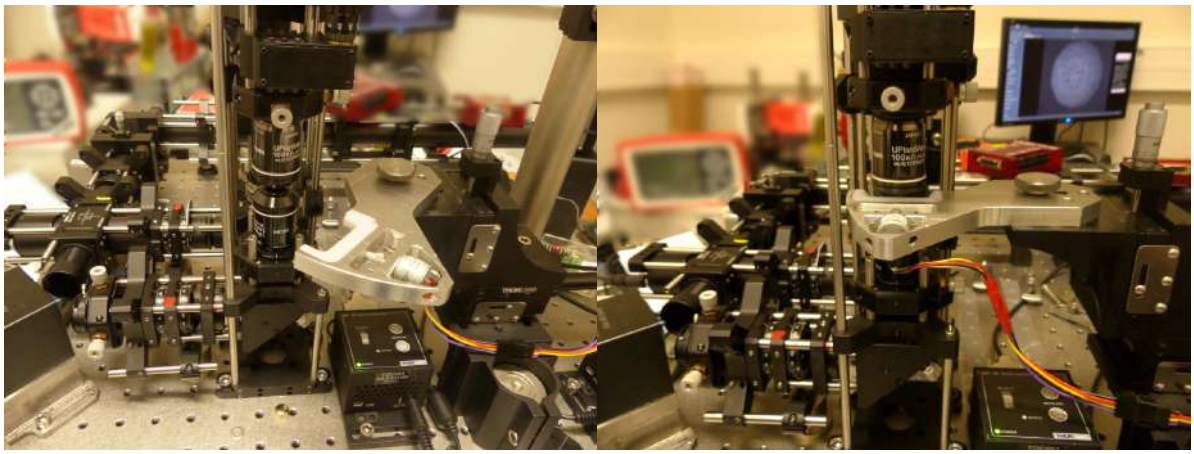

Figure S2: specific sample holder to perform specimen rotation using an optical fiber connected to a stepper motor, the sample being attached to the fiber by photopolymeriztion (see section d)

In order to perform sample rotation within the narrow space between the condenser-objective, and the detection-objective, we have developed a specific rotation stage depicted in Figure S2. A rotating arm permits to carefully insert the sample, attached to an optical fiber (see Section 4). The fiber is inserted into a fiber cannula, which is connected to a stepper motor, driven via a LabJack U12 module. Immersion oil between both objectives ensures optical contact.

After each TDM with illumination rotation, a sample rotation is performed, and a new TDM dataset is acquired.
Data fusion for isotropic resolution is performed off-line (see Section 3).

2. Estimation of the resolution

As pointed out by Horstmeyer, *et al.* [5], measuring the resolution in coherent imaging may be challenging, and poses specific problems, especially if one wants to compare resolution obtained with different systems. For measuring lateral resolution, they consequently recommend the use of Siemens star targets, in either amplitude or phase, and propose a standardized method of resolution measurement. To generalize the method, such targets, extended in three dimensions (a Siemens 3-D star) should ideally be used, but are not, to the best of our knowledge, presently available. Throughout this work, we therefore stick to a simpler method, which, while obviously being less rigorous, permits a reasonable estimation of the 3-D resolution of our setup.
We have adopted the method already used in Ref. [6] to estimate resolution, fitting profiles obtained by cutting through the fiber, following the technique proposed by Bentzen [7] to align the profiles, and using the Python Imfit routine considering an edge profile [8]. The estimated σ from the edge profile is then multiplied by 2.355 to obtain the resolution [6]. Figure S3(a) shows the result obtained from Fig. 2(a) of the article. The method estimates a resolution of 95 nm using a 475 nm laser and with a numerical aperture of 1.4 at both illumination and detection, or $\lambda/3.5$NA (as in Ref. [6], but with shorter wavelength laser).

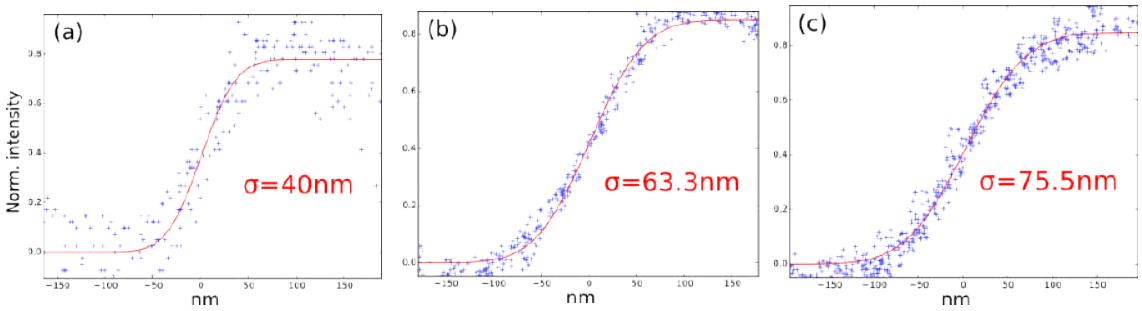

Figure S3: edge fit obtained on accumulated cuts through the tapered optical fiber. (a): lateral fit in TDM-IR. (b) lateral fit in TDM-IRSR. (c) longitudinal fit in TDM-IRSR. The resolution scales as 2.355σ.

After data fusion of 4 views, a lateral resolution of 149 nm is estimated (Fig. S3(b)) This result indicates that the fusion process is not fully optimal, slightly degrading the lateral resolution in the final image, but the obtained longitudinal resolution is estimated at 177 nm (Fig. S3(c)), demonstrating an almost isotropic 3-D resolution, which explains the very noticeable improvement in image quality observed on Figs. 2(e,f), Figs. 3(e-h) and Fig. 4 of the main article.

3. Data fusion

In order to obtain an image of the observed sample with isotropic resolution, data from the successive tomographic views obtained by rotating the specimen have to be recombined. The process requires several steps: hologram correction, 3-D stacks registration, Fourier data normalization, and final image reconstruction.
All computations are performed on a Linux PC, equipped with an Intel quadcore i7 processor (3.2 GHz), with 16 Gbytes of DDR3 memory, and programmed in C++ using open source libraries (FFTW, OpenCV) for the CPU reconstructions, and with CUDA library for GPU computations [9], performed on an NVidia Tesla C2075 card [10].

Hologram correction
Because residual aberrations will deteriorate the reconstructed images, each hologram is pre-processed with the method described in [11], simply adapted to transmission microscopy. Indeed, as our system is designed to observed a single object, attached to the rotating device, a large part of the field of view is empty, and can be used as reference background to measure the aberrations of the entire optical setup, using a polynomial fit. The aberrations, computed for each angle of illumination, are then simply subtracted from the corresponding hologram.
Then, a single view of the observed sample is computed from the holograms obtained by angular scanning of the illumination, as in [1-4]. Sample rotation is performed, and a new view of the specimen is obtained. The several images of the sample are then to be recombined. To do so, two steps are necessary, volume registration, performed in image space, and data normalization, performed in Fourier space.

Volume registration
Taking into account the speed of acquisition of our system (typically 6s seconds per view), the considered specimens under observation do not experience changes in morphology. However, unwanted translations or rotation conicity affect in practice the purely rotational desired movement. These parasitic movements may result from mechanical constraints imposed by the stepper motor onto the rotation device, or onto the fiber, and which slowly release, or from slight misalignment of the fiber with the motor rotation axis (conicity).
From an imaging point of view, one can therefore consider that the different images of the samples are connected by rigid transforms. Consequently, one must identify the parameters of these transforms before image registration and fusion. The problem is very similar to that encountered for example in SPIM microscopy [12], that also takes benefit of specimen rotation to obtain a final improved image of the observed sample, and for which specialized registration methods have been developed in order to automatically compute data registration [13,14]. Such methods, which rely on the inclusion of fluorescent micro-beads, embedded as landmarks for image registration [14], or which include a deconvolution process [13], are therefore not adapted to our problem.
We therefore simply adopted the methods used in PET or MRI imaging [15], as implemented through the AIR software [16], compiled for our Linux computer. Using AIR libraries, a pre-segmentation of the images and an adjustment of input variables of the registration process allow for automatic determination of the rigid transform parameters. Then, each volume can be registered in its own reference frame, properly rotated with respect to the first images, and corrected for parasitic movements.
Data normalization
In TDM-IR, when varying the direction of illumination with a tip-tilt mirror, inevitable phase shifts of the illumination beam are induced. This renders necessary to correct the sample frequencies measured in Fourier space for each direction of illumination, which is easily performed by normalizing the data with respect to the specular beam [1,3,11]. This allows for obtaining a coherent subset of data before the final 3-D Fourier transform giving one image of the specimen.
When also rotating the specimen, after the necessary volume registration, a similar correction is to be performed between the different views of the sample: for example, a translation in the spatial domain corresponds to a multiplication of the frequencies by a phase ramp. Therefore, each volume is normalised again with respect to the zero frequency after registration. This allows for obtaining several views of the sample, which are correctly positioned in space, and coherent with each other, not only in intensity, but both in amplitude and in phase. Then, the Fourier components corresponding to each view can be assembled.

Frequency overlapping

When adding the Fourier components, we take benefit from the fact that lower frequencies are recorded several times, which permit to average them and improve the signal to noise ratio in the final images. As an example, Figure S4 shows two frequency supports, corresponding to two views acquired at 0° and after a 90° sample rotation. The central part in purple highlights the frequencies, which are in that case recorded twice.

So, the whole data fusion process in TDM-IRSR requires working both in the spatial domain for the volumes registration and in the Fourier domain for correctly merging data.

Time consumption of the procedure

The most critical point for correct volume registration is the identification of good landmarks, used to compute the rigid transforms. For Fig. 2 (4 angles) and Fig. 3 (8 angles for the crystal) of the manuscript, this step was performed manually.

For the pollen grain images displayed on Fig. 4 of the manuscript, 10 successive views have been merged, and the reconstruction was fully automatic, which required 30 min for automatic rigid transforms determination with AIR, 6 min for images registration (real part, imaginary part, OTF, normalization), and 20 min for the final image fusion. The final rendering for Vizualizations 2-4 is about 30 s with Blender. Note that the programs for the multi-view, isotropic-resolution setup have not been optimized, contrary to the programs used for single view reconstruction [17].

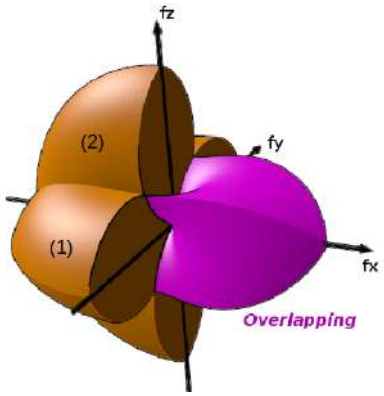

Figure S4: Illustration of the overlapping frequencies when recording two views of the same object. (1): frequencies for first view. (2): frequencies after 90° sample rotation. Purple: common frequencies.

4. Sample preparation

The fabrication of the microtip used as a sample holder was based on a self-guiding photopolymerization process at the extremity of an optical fibre as depicted in Refs. [18,19]. In this particular case, the monomer used was pentaerythritol triacrylate (PETIA), a tri-functional acrylate monomer and the photo-initiator was bis(2,4,6-trimethylbenzoyl)-phenylphosphineoxide, supplied by BASF under the brand name Irgacure 819 (2 wt %). This compound can initiate radical polymerization when illuminated at 375 nm.

The optical set-up used for holder fabrication is presented on Figure S5. First, a laser diode (375 nm, 60 mW) was coupled by an objective to a single mode optical fibre (SMF28e) with a 9 µm core diameter. The light emerging from the opposite extremity is used to initiate photopolymerization. The coupling was adjusted to obtain an output power of 5 mW.

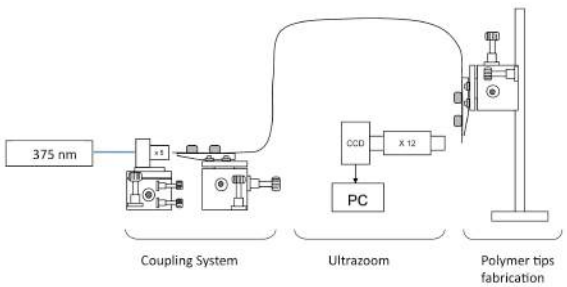

Figure S5: Optical set-up used for microtip fabrication and attachment microscopic samples to the microtip (see figures S6 and S7)

Figure S6 describes the fabrication of the tip, and attachment of a sample. The light guided in the fibre can initiate polymerization. A self-guiding process confines the polymerization to create a polymer tip with a diameter equal to the fibre core. After exposure, the fibre was rinsed in ethanol and a polymeric tip was visible as an extension of the fibre core (steps a to f of Figure S6).

The second step consisted in gluing the specimen to this holder. The microtip was dipped again in the formulation (step g), taking care that the formulation did not embed the whole holder but only its very end of the tip (step h). As in the first step, a small quantity of formulation remained at the extremity of the holder. Then, the specimen to study was placed under the holder and the holder extremity was displaced

on top of the specimen (step i). A new exposure to the laser light polymerized the tiny formulation drop and glued the specimen to the holder (step j).
Finally, the fibre is removed from the setup to be cut, and inserted in the rotation device described in Section a (step k).

Figure S7 shows actual images of the process (steps b, c, g, k) when attaching a pollen grain to the optical fibre. Note that in this example, the laser was kept on after the attachment process, and, as UV light is used to cure the resin, the pollen fluoresces, and is therefore visible as a reddish spot.

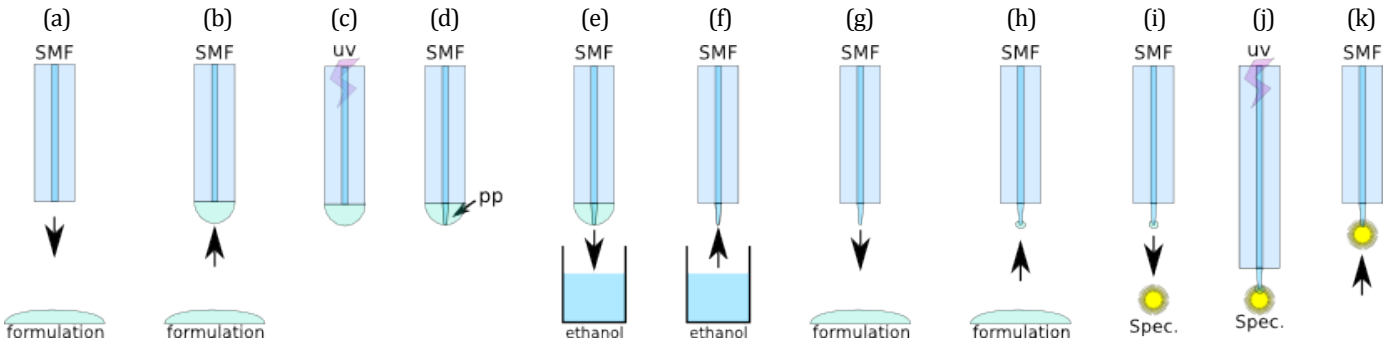

Figure S6: step by step attachment of a microscopic specimen to an optical fibre: microtip fabrication at the extremity of a single mode fibre and specimen gluing.

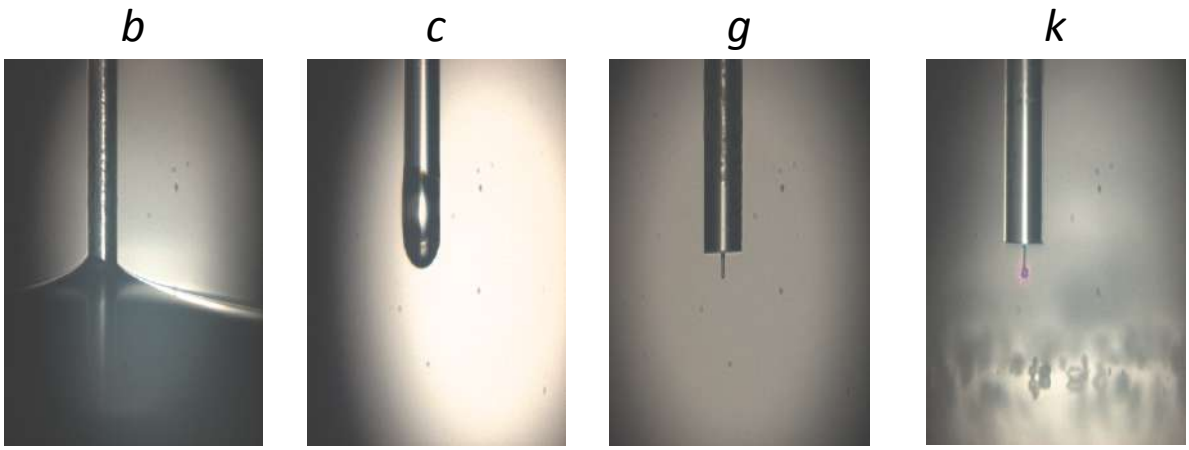

Figure S7: actual captures of steps b, c, g and k, when attaching a pollen grain to an optical fibre. The pollen is fluorescing and therefore visible in red on image k, as UV light is used for photopolymerisation.

References

1. V. Lauer, J. Microscopy **205**, 165 (2002)
2. W. Choi, C. Fang-Yen, K. Badizadegan, S. Oh, N. Lue, R. R. Dasari, and M. S. Feld, Nature Meth. **4**, 717 (2007)
3. M. Debailleul, B. Simon, V. Georges, O. Haeberlé, and V. Lauer, Meas. Sci. Technol. **19**, 074009 (2008)
4. Y. Cotte, F. Toy, P. Jourdain, N. Pavillon, D. Boss, P. Magistretti, P. Marquet, and C. Depeursinge, Nature Phot. **7**, 113 (2013)
5. R. Horstmeyer, R. Heintzmann, G. Popescu, L. Waller, and C. Yang, Nature Phot. **10**, 68 (2016)
6. M. Debailleul, V. Georges, B. Simon, R. Morin and O. Haeberlé, Opt. Lett. **34**, 79 (2009)
7. S. M. Bentzen, Med. Phys. **10,** 579 (1983)
8. http://cars9.uchicago.edu/software/python/lmfit/builtin_models.html
9. NVidia, NVIDIA's Next Generation CUDA Compute Architecture : Fermi - Whitepaper. NVidia Inc., 2011
10. NVidia, NVIDIA TESLA C2075 Companion Processor. NVidia Inc., 09 2011.
11. H. Liu, J. Bailleul, B. Simon, M. Debailleul, B. Colicchio and O. Haeberlé, Appl. Opt. **53**, 748 (2014)
12. P. J. Ververr, J. Swoger, F. Pampaloni, K. Greger, M. Marcello, and E. H. K. Stelzer, Nature Methods **4**, 311 (2007)
13. F. Preibisch, F. Amat, E. Stamataki, M. Sarov, R. H. Singer, E. Myers, and P. Tomancak, Nature Methods **11 ,** 645 (2014)
14. F. Preibisch, S. Saalfeld, J. Schindelin, and P. Tomancak, Nature Methods, **7**, 418 (2010)
15. RP. Woods, S.R. Cherry, and J.C. Mazziotta, J. of Comp. Assis. Tomography **16**, 620 (1992)
16. freely dowloadable at http://bishopw.loni.ucla.edu/AIR5/
17. J. Bailleul, B. Simon, M. Debailleul, H. Liu, and O. Haeberlé, Proc. SPIE **8437**, Paper 8437-7 (2012)
18. R. Bachelot, R. Bachelot, C. Ecoffet, D. Deloeil, P. Royer, and D.-J. Lougnot, Appl. Opt. **40**, 5860 (2001)
19. S. Jradi, O. Soppera, D.-J. Lougnot, R. Bachelot, and P. Royer, Opt. Mat. **31**, 640 (2009)